

Article

NO and CO Emission Characteristics of Laminar and Turbulent Counterflow Premixed Hydrogen-Rich Syngas/Air Flames

Lei Cheng ^{1,†}, Yanming Chen ^{2,†} , Yebin Pei ¹, Guozhen Sun ², Jun Zou ², Shiyao Peng ^{1,*} and Yang Zhang ^{2,*}¹ Pipe China Institute of Science and Technology, Tianjin 300450, China² Shanxi Research Institute for Clean Energy, Tsinghua University, Taiyuan 030032, China* Correspondence: pengsy01@pipechina.com.cn (S.P.); yang-zhang@tsinghua.edu.cn (Y.Z.);
Tel.: +86-316-217-6290 (S.P.); +86-10-6277-3153 (Y.Z.)

† These authors contributed equally to this work.

Abstract: Burning hydrogen-rich syngas fuels derived from various sources in combustion equipment is an effective pathway to enhance energy security and of significant practical implications. Emissions from the combustion of hydrogen-rich fuels have been a main concern in both academia and industry. In this study, the NO and CO emission characteristics of both laminar and turbulent counterflow premixed hydrogen-rich syngas/air flames were experimentally and numerically studied. The results showed that for both laminar and turbulent counterflow premixed flames, the peak NO mole fraction increased as the equivalence ratio increased from 0.6 to 1.0 and decreased as the strain rate increased. Compared with the laminar flames at the same bulk flow velocity, turbulent flames demonstrated a lower peak NO mole fraction but broader NO formation region. Using the analogy theorem, a one-dimensional turbulent counterflow flame model was established, and the numerical results indicated that the small-scale turbulence-induced heat and mass transport enhancements significantly affected NO emission. Considering NO formation at the same level of fuel consumption, the NO formation of the turbulent flame was significantly lower than that of the laminar flame at the same level of fuel consumption, implying that the turbulence-induced heat and mass transfer enhancement favored NO_x suppression.



check for updates

Citation: Cheng, L.; Chen, Y.; Pei, Y.; Sun, G.; Zou, J.; Peng, S.; Zhang, Y. NO and CO Emission Characteristics of Laminar and Turbulent Counterflow Premixed Hydrogen-Rich Syngas/Air Flames. *Processes* **2024**, *12*, 475. <https://doi.org/10.3390/pr12030475>

Academic Editor: Cherng-Yuan Lin

Received: 29 December 2023

Revised: 2 February 2024

Accepted: 8 February 2024

Published: 26 February 2024



Copyright: © 2024 by the authors. Licensee MDPI, Basel, Switzerland. This article is an open access article distributed under the terms and conditions of the Creative Commons Attribution (CC BY) license (<https://creativecommons.org/licenses/by/4.0/>).

Keywords: hydrogen-rich syngas; counterflow flame; NO emission; turbulence

1. Introduction

Hydrogen-rich syngas fuels, with their wide availability and abundant quantity, offer a promising alternative to conventional gaseous fuel in the industry [1,2]. The full utilization of hydrogen-rich syngas fuels is a potential way to reduce the reliance on natural gas in the heat and power supply system. NO_x emission from the combustion of hydrogen-rich syngas fuels is an important concern in both the academic and industrial sectors. Understanding the characteristics of NO_x formation is of great significance for the achievement of clean and efficient combustion technologies.

Extensive studies have been conducted in the literature on NO_x formation during the combustion process of hydrogen-rich syngas fuels. It is generally accepted that NO_x formation in hydrogen-rich flames receives two main influences. The first influence is that hydrogen has a higher combustion temperature than natural gas at the same equivalence ratio, and the richness of hydrogen in the fuel may result in a higher flame temperature and thereby higher thermal NO_x formation [3]. The second influence is that the existence of abundant hydrogen in the fuel extends the lean combustion limit, and the hydrogen-rich flames can be sustained under leaner conditions. Ultra-lean combustion favors NO_x suppression and higher combustion efficiency [4]. For example, Tuncer et al. [5] studied hydrogen-enriched natural gas combustion in a gas turbine combustor and found that an increase in the hydrogen proportion in the fuel results in a more stable flame at a

lower equivalence ratio, leading to a reduction in overall NO_x emission. Calabria et al. [6] numerically studied the performance of various fuels in a T100 gas turbine and also found that an increase in hydrogen helps establish ultra-lean combustion, favoring NO_x suppression. Reale [7] increased the proportion of hydrogen and reduced the production of NO_x by adding water vapor for dilution.

In order to insightfully understand the mechanism of NO formation and consumption, lab-scale fundamental flames with well-defined boundary conditions are needed. Among a group of lab-scale flames, the counterflow flame is a good platform to study NO formation, as the key parameters influencing the NO formation, such as the temperature, equivalence ratio, strain rate, etc., can be separately controlled in this configuration. Previous studies indicated that in laminar counterflow flames, an increase in hydrogen content leads to an increase in NO emission [8]. Shi et al. found that a higher strain rate reduces NO emission [9]. In addition, Xi et al. conducted numerical studies on NO generation in methane (CH₄)/n-heptane (n-C₇H₁₆) dual-fuel laminar counterflow flames [10,11]. They found that NO decreases with an increase of an equivalent ratio under fuel-rich conditions, and the NO in Xi et al.'s studies was mainly prompt NO [10]. Moreover, NO emission is also related to the peak flame temperature, heat release rate, and pressure [12]. NO emission indices have been obtained, and it has been observed that the NO emission index decreases with an increase in pressure [12].

Additionally, for most combustion devices, combustion is organized under turbulent combustion conditions to increase the power density. As per the comparison between the characteristic turbulent scale and flame scale, the combustion is categorized into different regimes [13]. For turbulent premixed flames, the well-known Borghi–Peters regime diagram [14] gives an insight into turbulence–flame interaction modes. The existing studies in the literature (e.g., [15]) proved that modern combustion devices are often operated in the thin-reaction-zone regime, in which the length scale of turbulent eddies is smaller than the thermal thickness of the laminar flame but larger than the thin reaction zone of the flame. In this regime, turbulent eddies penetrate into the preheat zone of the flame, affecting heat and mass transfer within the flame and thus influencing combustion products [16]. Investigating the emission characteristics of pollutants under turbulent effects is of practical significance. Ren et al. [17] studied the impact of small-scale turbulence on premixed flame NO_x formation and proposed a model to simulate NO_x generation in turbulent lean premixed combustion. Ren's model indicates that NO_x formation at the flame front decreases as turbulence intensity increases. Aladawy et al. [18] conducted a study on the impact of turbulence intensity on NO_x emissions using methane/air as fuel. Their analysis revealed that turbulence intensity only affects NO_x generation in the flame zone, while its influence on the post-flame region can be disregarded. Hwang et al. [19] concluded that the amount of NO generation decreases with both strain rate and turbulence intensity. However, there is still no consensus in the literature regarding the influence of turbulent eddies on NO_x formation, requiring further studies under well-defined boundary conditions.

Based on the aforementioned considerations, the objective of this study is to investigate NO formation during the combustion process of hydrogen-rich syngas fuels. Unlike the aforementioned studies, we established both the laminar and turbulent counterflow flame configurations with well-defined turbulent boundary conditions, and we measured NO and CO emission with respect to equivalence ratio and flow characteristics. With these well-established configurations, the effects of small-scale turbulence, bulk flow strain rate, and fuel properties are decoupled and insightfully investigated. We also simulate NO and CO formation using a one-dimensional counterflow flame model integrated with a detailed chemical kinetic model. The findings of this study provide theoretical guidance for the design of combustion devices fueled with hydrogen-rich syngas fuels.

2. Methods

2.1. Fuel Composition and the Counterflow Flame Experimental Method

The fuels used in the present study included two typical hydrogen-rich syngas fuels. The gas composition and heat value of the two syngas fuels are shown in Table 1. Fuel 1 represented the syngas obtained through the entrained-flow gasification of pulverized coal and oxygen (e.g., [20]), while Fuel 2 represented the syngas produced through the fluidized-bed gasification of water-coal slurry and air (e.g., [21]).

Table 1. The components and calorific value of fuel gas.

Fuel	Components by Volume/%					Calorific Value/(MJ·Nm ⁻³)
	H ₂	CO	CH ₄	N ₂	CO ₂	
Fuel 1	24	66	0	4	6	10.9
Fuel 2	20	24	3	44	9	6.3

These two types of syngas fuels were chosen to represent different gasification methods and feedstocks, enabling a comprehensive analysis of NO and CO emissions in hydrogen-rich syngas flames. By studying the emission characteristics of these fuels, valuable insights can be gained into the environmental impact of hydrogen-rich syngas combustion and potential ways to mitigate harmful emissions.

Figure 1 schematically depicts the experimental system used in this study. The core component of the system is the counterflow burner. It consists of upper and lower nozzles positioned symmetrically with a separation distance of 2 cm ($L = 2$ cm). The nozzle outlet has an inner diameter of 1 cm. To control the flow rates of different gas streams, mass flow meters are employed in the gas supply system. The upper nozzle is supplied with nitrogen as the main gas stream, while the lower nozzle receives a mixture of air and syngas fuel at a specific equivalence ratio. Both the upper and lower nozzles are designed to provide co-flow shielding using nitrogen (N₂) gas. This shielding action helps to confine the flame and minimize its interference with the surrounding ambient air. As a result, flame stability is improved, and experimental errors are reduced. Considering the small spacing between the nozzles and the high temperature of the flame, water cooling systems are incorporated to prevent overheating during prolonged experiments. These cooling devices ensure that the burner remains within safe operating temperatures. Depending on the experimental requirements, the flow field inside the nozzles can be conditioned differently. For laminar flow, sintered metal plates are placed inside the nozzles as laminar screens. These plates aid in achieving the desired laminar flow conditions. Conversely, for turbulent flow, a turbulence generator plate with multiple holes is installed in the lower nozzle. This plate generates well-defined fully developed turbulence, allowing researchers to study turbulent combustion with specified boundary conditions. To measure the average fluctuation velocity at the nozzle exit, a hot-wire anemometer operating at a frequency of 150 kHz is employed. This measurement provides valuable data on the flow characteristics of the combustion process.

The flow rates of fuel Q_{fuel} , air Q_{air} , and nitrogen Q_{N_2} were individually controlled using a set of mass flow meters (ACCU, $\pm 1.0\%$ F. S) pre-calibrated using a high-accuracy wet gas meter (W-K-10B, $\pm 0.1\%$ F. S). The flow rates in the present work were estimated within $\pm 0.4\%$ according to the calibration data. The pollutants generated during the combustion process were sampled using a water-cooled sampling probe. The sampling position is located along the nozzle axis and was moved up and down to measure the axial distribution of the NO and CO. The outer diameter of the sampling probe needle was less than 0.5 mm to minimize the flow field disturbance induced by the probe needle. The inner diameter of the sampling probe needle was less than 0.1 mm, and great efforts were made to ensure isokinetic sampling, minimizing its impact on the flame. The sampled mixture was analyzed using a flue gas analyzer (Thermo Scientific 48i/42i, Thermo Fisher Scientific, Waltham, MA, USA). Among them, the Thermo Scientific flue gas analyzer has a

mole fraction measuring range of $0\sim 100 \times 10^{-6}$ for NO and $0\sim 1000 \times 10^{-6}$ for CO, and the measuring uncertainty is less than $\pm 1\%$.

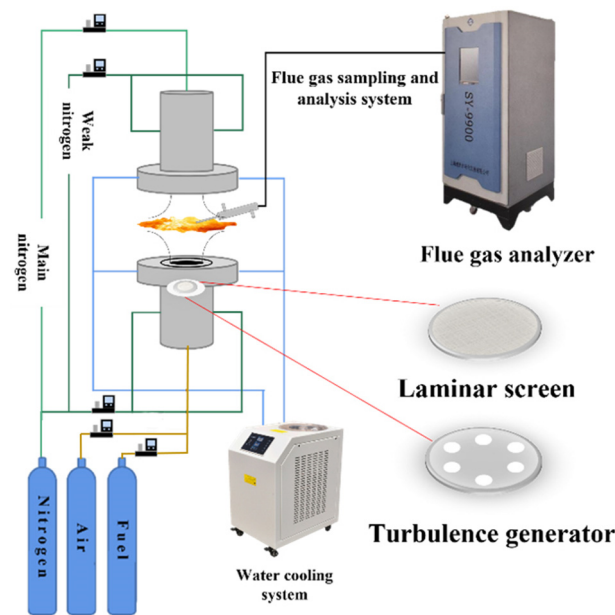


Figure 1. Schematics of the s counterflow flame system.

In the experiment, the nozzle outlet flow velocity was controlled by controlling the gas flow rate, so as to change the experimental equivalent ratio ϕ and the bulk flow strain rate κ . The bulk flow strain rate κ was determined using Equation (1) [22].

$$\kappa = \frac{U_l}{L} \left[1 + \frac{U_l \sqrt{\rho_l}}{U_u \sqrt{\rho_u}} \right] \quad (1)$$

where L is the nozzle separation distance; U_u and U_l are the average flow rates of the upper and lower nozzles, respectively. ρ_u and ρ_l are the average gas density of the upper and lower nozzle, respectively.

2.2. Experimental Uncertainties

The experimental uncertainties were carefully addressed in the present study. The uncertainty (δ) of the measured NO and CO mole fractions, X_{NO} and X_{CO} , was estimated as per Moffat's theory [23], expressed as Equation (2).

$$\delta_{X_i} = \sqrt{B_{X_i}^2 + [t(\eta)\sigma_{X_i}]^2} \quad (2)$$

where B_{X_i} represents the fixed error of X_i determined by the uncertainty of X_i of the measurement instruments. In the present study, the uncertainty of the flue gas analyzer was $\pm 0.1\%$. σ_{X_i} represents the standard deviation of multiple measurements of random uncertainty X_i . $t(\eta)$ is the Student's t statistic appropriate for the number of samples η and the confidence level desired.

The equivalent ratio ϕ and the bulk flow strain rate κ were indirect measurement values. As per the uncertainty transfer theory [24], the uncertainties of ϕ and κ were estimated using Equations (3) and (4).

$$\delta_\phi = \sqrt{\left(\frac{\partial \phi}{\partial f_{\text{fuel}}} \delta_{f_{\text{fuel}}} \right)^2 + \left(\frac{\partial \phi}{\partial f_{\text{air}}} \delta_{f_{\text{air}}} \right)^2} \quad (3)$$

$$\delta_{\kappa} = \sqrt{\left(\frac{\partial \kappa}{\partial U_{low}} \delta U_{low}\right)^2 + \left(\frac{\partial \kappa}{\partial U_{up}} \delta U_{up}\right)^2} \quad (4)$$

where f denotes the flow rate. The uncertainties of flow rate and velocity were determined by the accuracy of the flow meters, being $\pm 0.5\%$ as per the calibration data. Thus, the uncertainties of ϕ and κ were estimated to be within 1%, too small to display in the figures hereafter.

The experimental conditions are listed in Table 2. As most of the practical industrial premixed burners are designed and operated under fuel-lean conditions for more complete consumption of the fuel and lower emissions, the ϕ values in the present study covered the range of 0.6–1.0 to provide a theoretical guide to the industrial application.

Table 2. Experimental conditions.

Fuel	Equivalent Ratio, ϕ	Strain Rate, (s ⁻¹)	Flame State
Fuel 1	0.6/0.8/1.0	154–355	Laminar/Turbulence
Fuel 2	0.6/0.8/1.0	75–289	Laminar/Turbulence

2.3. Numerical Simulation

The conditions of the numerical simulation model were consistent with those in the experiments. Figure 2 illustrates the schematic diagram of the counterflow flame model in the simulation and flame structure. The opposed jet flows created a stagnation surface between the nozzles, which allowed for the mathematical simplification of the actual flow as one-dimensional along the nozzle axis.

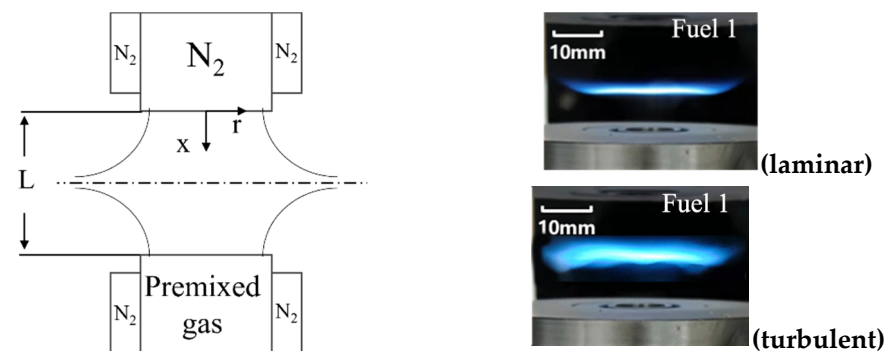


Figure 2. Model of counterflow diffusion flame and flame structure.

The counterflow flames were simulated using the 1D OPPDIF model [25] with modifications to account for the turbulence. This model was integrated with the Sandia CHMKIN II [26] and the Transport [27] sub-routines. To be more specific, for laminar flames, the conservation equations were established in cylindrical coordinates, as Equations (5)–(8).

Mass conservation equation:

$$\frac{\partial(\rho u)}{\partial x} + \frac{1}{r} \frac{\partial(\rho v r)}{\partial r} = 0 \quad (5)$$

Energy conservation equation:

$$\rho u \frac{dT}{dx} - \frac{1}{C_p} \frac{d}{dx} \left(\lambda \frac{dT}{dx} \right) + \frac{\rho}{C_p} \sum_k C_{pk} Y_k V_k \frac{dT}{dx} + \frac{1}{C_p} \sum_k h_k \dot{\omega}_k + \frac{1}{C_p} \dot{Q}_{rad} = 0 \quad k = 1, \dots, K \quad (6)$$

Species conservation equation:

$$\rho u \frac{dY_k}{dx} + \frac{d}{dx} (\rho Y_k V_k) - \dot{\omega}_k W_k = 0 \quad k = 1, \dots, K \quad (7)$$

Axial momentum equation:

$$H - 2 \frac{d}{dx} \left(\frac{-\rho uv}{2r} \right) + \frac{3v^2}{r^2} + \frac{d}{dx} \left[\mu \frac{d}{dx} \left(-\frac{v}{r} \right) \right] = 0 \quad (8)$$

where H satisfies Equation (9) and V_k satisfies Equations (10) and (11).

$$H = \frac{1}{r} \frac{\partial p}{\partial r} = \text{constant} \quad (9)$$

$$V_k = -\frac{1}{X_k} D_{km} \frac{dX_k}{dx} - \frac{D_k^T}{\rho Y_k T} \frac{1}{dx} \frac{dT}{dx} \quad (10)$$

$$D_{km} = \frac{1 - Y_k}{\sum_{j \neq k}^K \frac{X_j}{D_{jk}}} \quad (11)$$

where ρ is the density; u and v are axial and radial velocities, respectively. λ is the thermal conductivity; μ is the dynamic viscosity; T is the temperature; C_p is the average specific heat capacity; Q_{rad} is heat loss caused by gas and particle radiation. For the k th component, C_{pk} is the heat capacity, Y_k is the mass fraction, V_k is the diffusion velocity, h_k is the specific heat enthalpy, $\dot{\omega}_k$ is the molar rate of chemical reaction per unit volume, and W_k is the molecular weight. D_{km} , D_{jk} , and D_k^T are the mixture-averaged diffusion coefficient, binary coefficient, and thermal diffusion coefficient, respectively.

For turbulent flames, our previous work [28] has validated that the turbulence generator used in the present experiment generated turbulent outlet boundary conditions dominated by viscous dissipation, and spectral analysis has demonstrated the rationality of assuming vigorous turbulence in the turbulence simulation. Therefore, for turbulent flames, this study adopted the concept of the “analogy theorem” in heat and mass transfer, in which the turbulence-induced heat and mass transfer enhancements were considered as the turbulent transport processes. In this case, the turbulent fluctuation terms were regarded as the enhancement of the heat and mass transfer. Thus, the method proposed by Ren et al. [17] was employed, in which the thermal conductivity λ , dynamic viscosity μ , and diffusion velocity V_k in laminar flame equations are replaced by λ' , μ' and V_k' , respectively, as expressed by Equations (12)–(14).

$$\lambda' = \lambda + \lambda_{turb} \quad (12)$$

$$\mu' = \mu + \mu_{turb} \quad (13)$$

$$V_k' = -\frac{1}{X_k} (D_{km} + D_{turb}) \frac{dX_k}{dx} - \frac{D_k^T}{\rho Y_k T} \frac{1}{dx} \frac{dT}{dx} \quad (14)$$

where λ_{turb} , μ_{turb} , and D_{turb} denote the equivalent transport induced by small-scale turbulence. In the present study, they are calculated using Equations (15)–(17).

$$\lambda_{turb} = Le_{turb} \rho C_p D_{turb} \quad (15)$$

$$\mu_{turb} = \rho C_\mu \frac{k^2}{\varepsilon} \quad (16)$$

$$D_{turb} = \frac{\mu_{turb}}{\rho Sc_{turb}} \quad (17)$$

where $k = 3 (u')^2 / 2$ is the turbulent kinetic energy; $\varepsilon = k^{3/2} / l_0$ is the turbulent dissipation rate; u' is the root mean square of the turbulent fluctuation velocity; l_0 is the integral scale of the turbulence; Sc_{turb} is the Schmidt number of turbulence; Le_{turb} is the turbulent Lewis number. In the experiment, the Reynolds number of nozzle exit flow with the nozzle outlet diameter as the characteristic length scale was within the range of 40–300. As mentioned in Section 2.1, turbulence was generated using a turbulence generator, so it was difficult

to determine its Reynolds number as the characteristic velocity and length scale were inaccessible. Nevertheless, the relative turbulent intensity characterized by the ratio u'/u was less than 27%, indicating that the turbulence was generally weak. Therefore, the proposed model based on the analogy theorem was acceptable for the present calculation. In the calculation, $Sc_{turb} = Le_{turb} = 1$, and $C_\mu = 0.5$ according to the experimental results. The integral scale l_0 was consistent with the experimental value from the derivation of the turbulent fluctuation velocity determined using a hot wire anemometer.

Grid independence verification is a crucial step in computational modeling to ensure reliable and accurate results. In this study, two grid sizes, 200 and 500, were selected to calculate the temperature distribution within the nozzle. The GRI Mech 3.0 [29] chemical kinetic model was used, and the experimental conditions, such as nozzle spacing (L), outlet temperature, and pressure, were matched at 2 cm, 293 K, and 1 atm, respectively. To assess the grid independence, the results obtained from both grid sizes were compared. Figure 3 illustrates the outcomes of this verification. It can be observed that the temperature distributions calculated using the two grid sizes were nearly identical. The peak temperature difference between the two grids was less than 3 K. Based on these findings, it can be concluded that a grid size of 200 is adequate for this study. The small discrepancy between the two grid sizes suggests that further refinement of the grid would not significantly impact the results. Therefore, using a grid size of 200 ensures computational efficiency while maintaining the accuracy required for the study.

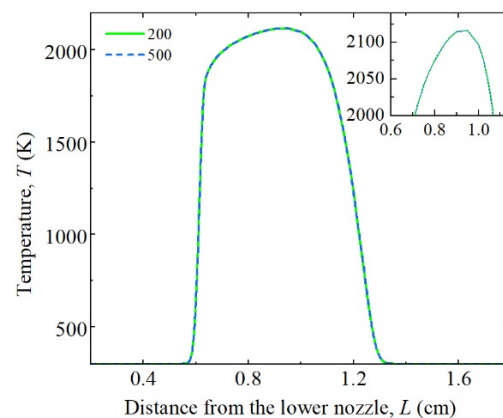


Figure 3. Test of grid independence.

3. Results and Discussion

3.1. NO/CO Emission Characteristics in Laminar Counterflow Flames of Hydrogen-Rich Syngas Fuels

The distribution patterns of NO/CO along the nozzle axis under laminar flow conditions are presented in Figure 4, showcasing a notable agreement between the simulated results and experimental data. When considering the same fuel type and equivalence ratio, the mole fraction of NO exhibits a distinctive trend—initially increasing and then decreasing with the elongation of the nozzle L , with the peak value occurring near the stagnation plane. As the strain rate κ increases, the NO distribution becomes narrower, accompanied by a decrease in the peak value. In parallel, the mole fraction of CO displays a monotonous decrease with increasing L . This behavior is expected, given that CO is part of the fuel and undergoes oxidation as it approaches the flame front. With an increase in the strain rate κ , the turning point where CO begins to decrease shifts towards the stagnation plane. This phenomenon can be attributed to higher gas velocity at the nozzle exit under elevated κ , resulting in a thinner laminar flame and lower temperature. Consequently, this leads to a significant reduction in thermal NO formation. The intricate interplay between strain rate, flame characteristics, and chemical reactions contributes to the observed variations in NO and CO distributions along the nozzle axis.

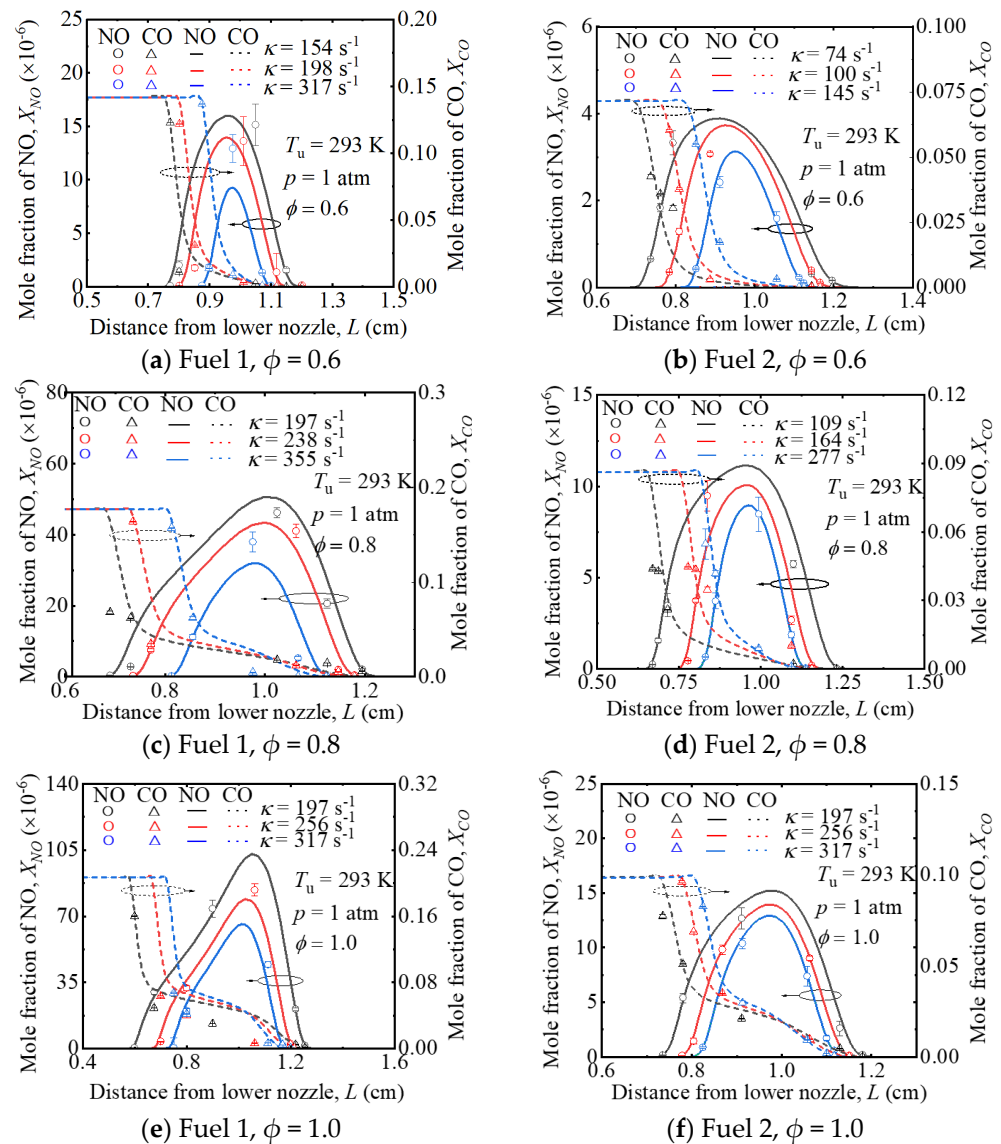


Figure 4. The variation in NO/CO mole fraction in laminar flame at various equivalent ratios and strain rates (circle and triangle symbols: experimental; lines: calculated).

For the same type of fuel, as the equivalence ratio ϕ increases, the mole fraction of NO significantly increases. This can be explained by the increased flame temperature as ϕ increases. The variation in CO mole fraction is featured in two categories. At lower equivalence ratios, as shown in Figure 4a,b,d, the CO mole fraction demonstrates a “one-stage” decrease as L increases; say X_{CO} initially decreases rapidly and then decreases slowly until it approaches zero. However, at a higher equivalence ratio, as shown in Figure 4c,e,f, the CO mole fraction shows a “two-stage” decrease as L increases. This indicates that the mole fraction of CO is affected by the combined effects of consumption and production. At a low equivalence ratio, the consumption rate of CO is higher than its production rate. Thus, CO rapidly decreases at the front of the flame. At a relatively higher equivalence ratio, the production of CO increases in the flame front, causing a two-stage CO decrease phenomenon.

For the same equivalence ratio and similar strain rate, significant differences also exist in NO/CO distribution between the two fuels. The NO and CO emissions for Fuel 1 are significantly higher than those for Fuel 2. This can be attributed to the substantial differences in the composition and flame temperature between the two fuels. Fuel 1 has a higher percentage of fuel contents, resulting in a higher flame temperature and more

thermal NO formation, resulting in a higher NO mole fraction. In addition, Fuel 1 has a higher CO composition, leading to a higher CO mole fraction across the flame front.

Figure 5 shows the peak flame temperatures under laminar flow conditions. Combined with Figure 4, it can be observed that the cases with higher peak flame temperatures also exhibit higher NO concentrations. This further confirms the findings mentioned above.

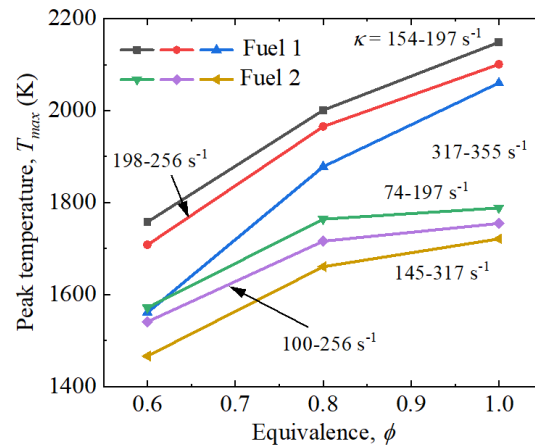


Figure 5. Variation in laminar flame peak temperature at various equivalence ratios.

3.2. NO/CO Emission Characteristics in Turbulent Counterflow Flames of Hydrogen-Rich Syngas Fuels

The conditions of the turbulent flames are listed in Table 3. Generally, the experimental results indicate that the turbulent flames exhibit a narrower range of flammability compared to the laminar flames. As shown in Table 3, the turbulent flames become unstable at a high strain rate or lean equivalence ratio.

Table 3. Turbulent flame experimental conditions.

Conditions	Fuel	Equivalence Ratio	Strain Rate	Flame Stability
Turbulent 1	Fuel 1	0.6	154 s ⁻¹	Unstable combustion
Turbulent 2	Fuel 1	0.6	198 s ⁻¹	
Turbulent 3	Fuel 1	0.6	317 s ⁻¹	
Turbulent 4	Fuel 1	0.8	197 s ⁻¹	
Turbulent 5	Fuel 1	0.8	238 s ⁻¹	
Turbulent 6	Fuel 1	0.8	355 s ⁻¹	
Turbulent 7	Fuel 1	1.0	197 s ⁻¹	
Turbulent 8	Fuel 1	1.0	256 s ⁻¹	
Turbulent 9	Fuel 1	1.0	317 s ⁻¹	
Turbulent 10	Fuel 2	0.6	75 s ⁻¹	Unstable combustion
Turbulent 11	Fuel 2	0.6	100 s ⁻¹	
Turbulent 12	Fuel 2	0.6	145 s ⁻¹	
Turbulent 13	Fuel 2	0.8	109 s ⁻¹	Unstable combustion
Turbulent 14	Fuel 2	0.8	164 s ⁻¹	
Turbulent 15	Fuel 2	0.8	227 s ⁻¹	
Turbulent 16	Fuel 2	1.0	197 s ⁻¹	
Turbulent 17	Fuel 2	1.0	241 s ⁻¹	
Turbulent 18	Fuel 2	1.0	289 s ⁻¹	

Similarly, the emission characteristics of turbulent flames were subjected to analysis, revealing that they exhibited analogous trends to laminar flames concerning variations in equivalence ratio and strain rate, as illustrated in Figure 6. For instance, considering NO formation, the mole fraction of NO decreases as the strain rate κ increases. This observed alignment between the simulated results and experimental data suggests that the turbulent

model employed in this study effectively captures the small-scale turbulence-induced heat and mass transfer enhancement. The agreement in trends implies that the turbulent flames respond similarly to changes in operating conditions as their laminar counterparts. In particular, the reduction in NO mole fraction with increasing strain rate highlights the role of turbulence-induced mechanisms in influencing the combustion process. The findings contribute to a comprehensive understanding of the emission characteristics of turbulent flames and underscore the applicability of the turbulent model for describing the intricate interplay of factors affecting heat and mass transfer in turbulent combustion.

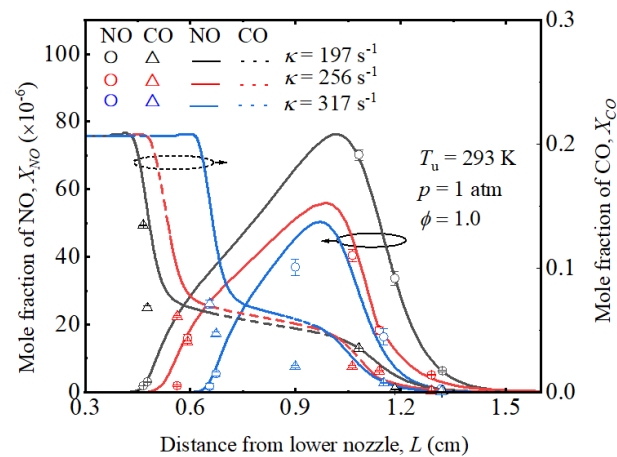


Figure 6. The variation in NO/CO mole fraction in turbulent flame with strain ratio ($\phi = 1.0$, Fuel 1; circle and triangle symbols: experimental; lines: calculated).

Figure 7 demonstrates the comparison between the emissions of laminar and turbulent counterflow flames under the stoichiometric condition ($\phi = 1.0$). It is seen that the peak NO mole fraction of the laminar flame is significantly higher than that of turbulent flame at the same κ and ϕ . The CO oxidation process is also faster in turbulent flames rather than in laminar flames, as the CO mole fraction decreases at an earlier stage as L increases in turbulent flames. This can also be partially explained by the increased flame thickness in turbulent flames.

Moreover, the NO mole fraction profiles become wider in turbulent flames compared to those in laminar flames. Thus, considering the overall NO_x formation across the flame, the integrated NO formation along the L direction is also given in Figure 7 (numbers near the curves). It is seen that the integrated NO value of the turbulent flame is quite close to—that is, only slightly lower than—that of the laminar flame, although the peak values are significantly different from each other.

Considering that the fuel consumption rate and combustion completeness in the turbulent flame differ from those in the laminar flame, an emission index of NO, EI_{NO} , is introduced in this section to evaluate NO formation at the same level of fuel consumption. EI_{NO} is calculated using Equation (18) [30].

$$EI_{NO} = \frac{-\int_0^L \dot{\omega}_{NO}(L)W_{NO}dL}{-\int_0^L \dot{\omega}_{fuel}(L)W_{fuel}dL} \times 1000 \quad (18)$$

where $\dot{\omega}_{NO}(L)$ and $\dot{\omega}_{fuel}(L)$ denote the mass production rates of NO and the fuel, respectively; W_{NO} and W_{fuel} denote the molecular weights of NO and the fuel, respectively.

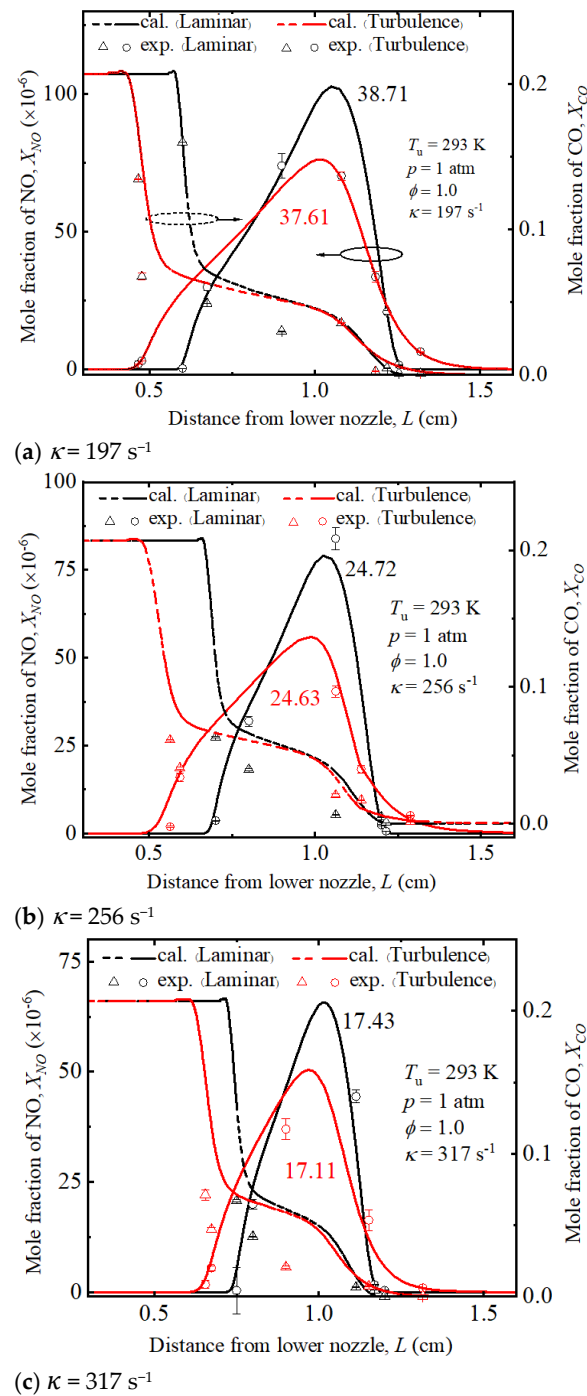


Figure 7. NO/CO mole fraction in laminar and turbulent flame at various strain rates ($\phi = 1.0$, Fuel 1; circle and triangle symbols: experimental; lines: calculated; numbers near the curves are the integrated values along the abscissa).

Figure 8 shows the variation in EI_{NO} as a function of the peak temperature T_{max} of the flame under various operating conditions. The EI_{NO} values of the laminar flames of different fuels under varied ϕ s generally converge on a single curve, and EI_{NO} exponentially grows as T_{max} increases. Similar results are found for turbulent flames. The EI_{NO} values of the turbulent flames follow another single curve of exponential growth as a function of T_{max} . These results indicate that the thermal NOx mechanism overwhelmingly dominates the NOx formation pathways in the flames in the present study. Additionally, a noteworthy phenomenon is that the EI_{NO} s of turbulent flames are significantly lower than those of lam-

in flames at the same T_{max} , implying that the turbulence-induced heat and mass transfer enhancement favors NO_x suppression. This is because the impact of turbulence on the combustion process leads to the difference in flame structure and substance concentration from laminar flow, and the heat and mass transfer caused by turbulence increases NO_x consumption. As a result, nitrogen oxide emissions are reduced.

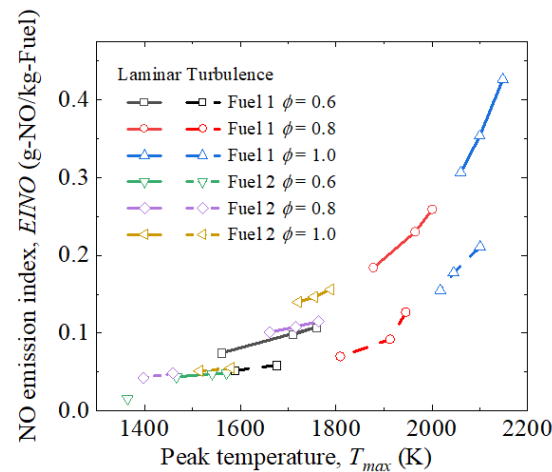


Figure 8. The variation in EI_{NO} as a function of the flame peak temperature at various equivalence ratios and strain rates.

Our findings on NO emission characteristics in hydrogen-rich syngas flames are a remarkable extension of the existing studies in the literature. Compared with the results found by Refs. [11–13] and Daniel et al. [31], the present study reaches similar results: that the higher strain rate leads to lower NO formation. Nevertheless, the present study obtained both the experimental and numerical NO formation in both turbulent and laminar counterflow flames at the same bulk flow velocity. To the best of the authors' knowledge, this study is the first one in the literature to experimentally compare NO formation in laminar and turbulent flames under the same bulk flow velocity. The effect of turbulence on NO formation in stretched counterflow flames is solely evaluated and turned out to be a high-impact factor.

4. Conclusions

In this study, we investigated the NO and CO emission characteristics of both laminar and turbulent counterflow hydrogen-rich syngas/air flames. The concluding remarks include the following:

- (1) Both laminar and turbulent counterflow premixed flames exhibit a similar trend of NO formation as a function of the equivalence ratio and strain rate. The peak NO mole fraction across the flame increases as the equivalence ratio increases from 0.6 to 1.0, and it decreases as the strain rate grows.
- (2) Turbulent flames demonstrate a lower peak NO mole fraction and wider NO mole fraction profile along the nozzle axis compared to laminar flames, and the integrated NO emission along the nozzle axis of the turbulent flame is only slightly lower than that of the laminar flame at the same equivalence ratio and strain rate. One-dimensional turbulent counterflow flame modeling indicates that the effect of small-scale turbulence on NO formation is due to enhanced heat and mass transfer.
- (3) Considering NO formation at the same level of fuel consumption, both laminar and turbulent flames exhibit an exponential growth in NO as a function of the flame temperature, indicating that the thermal NO mechanism dominates NO formation in the counterflow premixed hydrogen-rich syngas/air flames. The NO formation of the turbulent flame is significantly lower than that of the laminar flame at the same

level of fuel consumption, which implies that the turbulence-induced heat and mass transfer enhancement favors NO suppression.

Author Contributions: Conceptualization, L.C., S.P. and Y.Z.; methodology, L.C. and Y.C.; software, J.Z.; validation, Y.P., G.S. and J.Z.; investigation, L.C., Y.C. and G.S.; writing—original draft preparation, L.C., Y.C. and G.S.; writing—review and editing, Y.Z.; supervision, Y.Z.; project administration, S.P.; funding acquisition, S.P. and Y.Z. All authors have read and agreed to the published version of the manuscript.

Funding: This research was funded by the Natural Science Foundation of China, grant number 52176116, and the Key Technologies of Hydrogen-Mixed Natural Gas Transportation by Pipeline in Service (PipeChina, project number DTXNY202203).

Data Availability Statement: The authors will make the data available on request.

Acknowledgments: The author Y.Z. receives financial support from the Innovation Seed Fund of Shanxi Research Institute for Clean Energy, Tsinghua University.

Conflicts of Interest: The authors declare no conflict of interest.

References

- Pashchenko, D. Hydrogen-rich gas as a fuel for the gas turbines: A pathway to lower CO₂ emission. *Renew. Sust. Energy Rev.* **2023**, *173*, 113117. [[CrossRef](#)]
- Kothari, R.; Buddhi, D.; Sawhney, R.L. Comparison of environmental and economic aspects of various hydrogen production methods. *Renew. Sust. Energy Rev.* **2008**, *12*, 553–563. [[CrossRef](#)]
- Mirhashemi, F.S.; Sadrnia, H. NO_x emissions of compression ignition engines fueled with various biodiesel blends: A review. *J. Energy Inst.* **2020**, *93*, 129–151. [[CrossRef](#)]
- Cho, E.S.; Chung, S.H. Improvement of flame stability and NO_x reduction in hydrogen-added ultra lean premixed combustion. *J. Mech. Sci. Technol.* **2009**, *23*, 650–658. [[CrossRef](#)]
- Tuncer, O.; Acharya, S.; Uhm, J.H. Dynamics, NO_x and flashback characteristics of confined premixed hydrogen-enriched methane flames. *Int. J. Hydrogen Energy* **2009**, *34*, 496–506. [[CrossRef](#)]
- Calabria, R.; Chiariello, F.; Massoli, P.; Reale, F. CFD analysis of Turbec T100 combustor at part load by varying fuels. In Proceedings of the ASME Turbo Expo 2015: Turbine Technical Conference and Exposition, Montréal, QC, Canada, 15–19 June 2015; p. V008T23A020. [[CrossRef](#)]
- Reale, F. Effects of steam injection on the permissible hydrogen content and gaseous emissions in a micro gas turbine supplied by a mixture of CH₄ and H₂: A CFD analysis. *Energies* **2022**, *15*, 2914. [[CrossRef](#)]
- Cecere, D.; Carpenella, S.; Giacomazzi, E.; Stagni, A.; Di Nardo, A.; Calchetti, G. Effects of hydrogen blending and exhaust gas recirculation on NO_x emissions in laminar and turbulent CH₄/Air flames at 25 bar. *Int. J. Hydrogen Energy* **2024**, *49*, 1205–1222. [[CrossRef](#)]
- Wang, S.X.; Wang, Z.H.; Roberts, W.L. Measurements and simulations on effects of elevated pressure and strain rate on NO_x emissions in laminar premixed NH₃/CH₄/air and NH₃/H₂/air flames. *Fuel* **2024**, *357*, 130036. [[CrossRef](#)]
- Xi, J.; Yang, G.; Guo, H.; Gu, Z. Numerical investigation on NO formation in laminar counterflow methane/n-heptane dual fuel flames. *Int. J. Hydrogen Energy* **2022**, *47*, 13143–13156. [[CrossRef](#)]
- Xi, J.; Yang, G.; Guo, H.; Gu, Z. A numerical investigation on the formation of NO₂ and N₂O in laminar counterflow methane/n-heptane dual fuel flames. *Energy* **2022**, *258*, 124875. [[CrossRef](#)]
- Li, S.; Ma, Y.; Xi, J.; Yang, G.; Cai, J.; Song, T. Numerical simulation study on NO generation characteristics of methane/n-heptane dual fuel counterflow flames under different pressures. *Int. J. Hydrogen Energy* **2024**, *49*, 1325–1335. [[CrossRef](#)]
- Steinberg, A.M.; Hamlington, P.E.; Zhao, X.Y. Structure and dynamics of highly turbulent premixed combustion. *Prog. Energy Combust. Sci.* **2021**, *85*, 100900. [[CrossRef](#)]
- Silva, M.; Liu, X.; Hlaing, P.; Sanal, S.; Cenker, E.; Chang, J.; Johansson, B.; Im, H.G. Computational assessment of effects of throat diameter on combustion and turbulence characteristics in a pre-chamber engine. *Appl. Therm. Eng.* **2022**, *212*, 118595. [[CrossRef](#)]
- Driscoll, J.F.; Chen, J.H.; Skiba, A.W.; Carter, C.D.; Hawkes, E.R.; Wang, H. Premixed flames subjected to extreme turbulence: Some questions and recent answers. *Prog. Energy Combust. Sci.* **2020**, *76*, 100802. [[CrossRef](#)]
- Jin, T.; Wang, X.J.; Luo, K.H.; Luo, K.; Fan, J.R. Effects of intense turbulence on NO formation in propagating planar premixed flame. *J. Eng. Thermophys.* **2018**, *39*, 2056–2061. (In Chinese)
- Ren, Z.Y.; Yang, H.T.; Lu, T.F. Effects of small-scale turbulence on NO_x formation in premixed flame fronts. *Fuel* **2014**, *115*, 241–247. [[CrossRef](#)]
- AlAdawy, A.S.; Lee, J.G.; Abdelnabi, B. Effect of turbulence on NO_x emission in a lean perfectly-premixed combustor. *Fuel* **2017**, *208*, 160–167. [[CrossRef](#)]

19. Hwang, C.H.; Lee, S.; Lee, C.E. The effect of turbulence intensity of ambient air flow on NO_x emissions in H₂/air nonpremixed jet flames. *Int. J. Hydrogen Energy* **2008**, *33*, 832–841. [CrossRef]
20. Zhao, Z.; Kong, W.; Zhang, X.; Liu, M.; Cui, P. Catalytic steam gasification of bituminous coal for syngas production with catalyst derived from calcium-rich construction demolition waste. *Fuel* **2024**, *359*, 130428. [CrossRef]
21. Tawanda, M.; Stefan, I.; Alireza, K. A progress insight of the formation of hydrogen rich syngas from coal gasification. *J. Energy Inst.* **2022**, *105*, 81–102. [CrossRef]
22. Chung, K.L. *Combustion Physics*; Cambridge University Press: Lakewood, NJ, USA, 2010; pp. 154–196. [CrossRef]
23. Moffat, R.J. Describing the uncertainties in experimental results. *Exp. Therm. Fluid Sci.* **1988**, *1*, 3–17. [CrossRef]
24. Rees, D.G. Review: [Untitled]. *J. R. Stat. Society Ser. D (Stat.)* **1993**, *42*, 74–75. [CrossRef]
25. Lutz, A.E.; Kee, R.J.; Grcar, J.F.; Rupley, F.M. *OPPDIF: A Fortran Program for Computing Opposed-Flow Diffusion Flames*; Sandia National Laboratories Report SAND; Sandia National Lab. (SNL-CA): Livermore, CA, USA, 1997; pp. 96–8243. [CrossRef]
26. Kee, R.J.; Rupley, F.M.; Miller, J.A. *Chemkin-II: A Fortran Chemical Kinetics Package for the Analysis of Gas-Phase Chemical Kinetics*; Report No. SAND89-8009; Sandia National Laboratories: Livermore, CA, USA, 1989. [CrossRef]
27. Kee, R.J.; Dixon-Lewis, G.; Warnatz, J.; Coltrin, M.E.; Miller, J.A. *A Fortran Computer Code Package for the Evaluation of Gas-Phase, Multicomponent Transport Properties*; Sandia National Laboratories Report No. SAND86-8246B; Sandia National Laboratories: Livermore, CA, USA, 1988.
28. Zou, J.; Li, Z.X.; Zhang, H.; Lv, J.; Zhang, Y. Extinction characteristics of premixed flames of typical hydrogen-rich fuel gas. *J. Tsinghua Univ. (Sci. Technol.)* **2023**, *63*, 585–593. (In Chinese)
29. Gregory, P.S.; David, M.G.; Michael, F.; Nigel, W.; Moriarty, B.E.; Mikhail, G.; Thomas, B.C.; Ronald, K.; Hanson, S.; et al. GRI-MECH 3.0. Available online: http://www.me.berkeley.edu/gri_mech/ (accessed on 28 December 2023).
30. Li, Y.Z.; Hu, G.; Liao, S.Y.; Yuan, C.; Zhang, Y. Effects of partial premixing on NO production in methanol/dimethyl ether counterflow flames. *Fuel* **2018**, *234*, 974–984. [CrossRef]
31. Daniel, E.T.; Krishna, P.S.; Fabian, M.; William, F.N. Extinction and NO formation of ammonia-hydrogen and air non-premixed counterflow flames. *Proc. Combust. Inst.* **2023**, *39*, 1803–1812. [CrossRef]

Disclaimer/Publisher’s Note: The statements, opinions and data contained in all publications are solely those of the individual author(s) and contributor(s) and not of MDPI and/or the editor(s). MDPI and/or the editor(s) disclaim responsibility for any injury to people or property resulting from any ideas, methods, instructions or products referred to in the content.